Research Square

Preprints are preliminary reports that have not undergone peer review.
They should not be considered conclusive, used to inform clinical practice,
or referenced by the media as validated information.

Keratoconus severity detection using LSTM and machine learning techniques

Sibel Tariyan Ozyer

sibel.tariyan@ankaramedipol.edu.tr

Ankara Medipol Üniversitesi

Article

Keywords: Keratoconus, irregular astigmatism, optical coherence tomography, Machine learning algorithms, long-short Term Memory, OCT images.

Posted Date: August 25th, 2026

DOI: https://doi.org/10.21203/rs.3.rs-10594757/v1

License: This work is licensed under a Creative Commons Attribution 4.0 International License.
Read Full License

Additional Declarations: No competing interests reported.

Keratoconus severity detection using LSTM and machine learning techniques

Sibel Tariyan Ozyer [1*]

[1*]Department of Computer Engineering, Ankara Medipol University, Ankara, 06050, Turkey .

Corresponding author(s). E-mail(s): sibel.tariyan@ankaramedipol.edu.tr;

Abstract

Keratoconus(KC) is a common degenerative condition of the cornea delineated by corneal steeping caused by corneal protrusion and thinning, impacting the quality of vision or simply affecting the vision negatively. In the early stages, non-surgical treatment options, such as spectacles and soft contact lenses can address vision problems. As the disease progresses, irregular astigmatism may require different treatment options. Screening progress of the condition takes place usually at vision-centres every 6 months. It can be done by using optical coherence tomography. Indeed, topographic profiles can be utilized to track the advancement of keratoconus. In this study, machine learning (ML) algorithms were employed to detect the severity of keratoconus in a step to monitor the disease. Two long-short Term Memory (LSTM) based models were applied on a dataset which contains the parameter values of patients' eyes obtained from OCT images with date information. One of the models works on one eye, and the second model considers the effect of both eyes on the progression of the disease. The reported test results are promising, demonstrating the effectiveness and applicability of the developed approach.

Keywords: Keratoconus, irregular astigmatism, optical coherence tomography, Machine learning algorithms, long-short Term Memory, OCT images.

1 Introduction

Keratoconus (KC) is a progressive corneal ectatic disorder characterized by localized stromal thinning and protrusion[1]. The cornea serves as the main optical element of the eye. It refracts the incoming light to aid in clear vision; The stroma layer of

the cornea is most prominent because it constitutes 90% of the total thickness and is formed by regularly arranged collagen lamellae stabilized by natural intermolecular cross-links. Disruption of this biomechanical integrity results in progressive corneal deformation and optical irregularity [2] [3]. As the disease progresses, localized thinning causes the cornea to bulge forward into a cone shape, and it does not refract light correctly. Thus, patients commonly experience blurred vision, glare, photophobia, and diminished well-being as the disease advances [3] [4] [5].

KC is now understood not to be caused by a single factor but by several factors involving genetic, environmental factors (e.g., eye rubbing, ultraviolet exposure), biomechanical instability, and inflammatory and proteolytic mechanisms. Recent findings suggest that they elevated inflammatory cytokines and activation of matrix metalloproteinases in KC, highlighting the contribution of inflammatory pathways to stromal degradation. These findings challenge the conventional characterization of keratoconus as a purely non-inflammatory condition [3].

The reported prevalence(per 100,000) of KC varies widely across regions. For instance, it is 0.3 in Russia [6], 2300 in India [7], 54 in the United States [8], and 3300 in Lebanon and Iran [7]. However, healthcare planners and strategists anticipate even greater occurrence rate as early and subclinical cases were frequently missed [9] [10] [11]. Better knowledge of the disease is required to help determine the required services to mitigate the resources and improve patient well-being [12].

Generally, KC develops during the teenage years in the early 20s through 30s and in many cases towards mid-30s for all ethnic backgrounds and genders [9], [13]. Progression rates tend to decline with age [9] [13] [10] [11]. The diagnosis of KC generally involves a thorough medical history, a physical examination, and corneal imaging techniques; while corneal topography was historically used for initial curvature assessment, corneal tomography and optical coherence tomography are now considered essential for early and subclinical detection, tomography, and optical coherence tomography are crucial for early subclinical detection [14] [15].

KC affects the quality of life from different perspectives [16], including healthcare, financial, driving, symptoms, career, enjoyment, and relationships [4]. Findings of another study confirmed that cross-linking is required for improving emotional well being, relieving symptoms, and limited activity improvement [5]. This illustrates how KC impacts life; monitoring the disease and predicting how it progresses is the key factor in deciding on the treatment approaches to be taken.

Clinically, KC severity is commonly graded using systems such as Amsler-Krumeich, CLEK, and ABCD classifications. Early detection of KC is critical because modern interventions can halt or slow disease progression. Visual correction with spectacles or contact lenses can provide clear vision and help patients avoid the potential need for intracorneal ring segments or corneal transplant surgery in subsequent stages [17].

The introduction of minimally invasive corneal collagen cross-linking (CXL) fundamentally changed how KC is treated by halting or slowing the progression of corneal ectasia particularly when applied from early to intermediate stages by creating new chemical bonds between collagen fibres in the stroma. Recently, IVMED-80 is another option for nonsurgical treatment for KC, while intrastromal lamellar keratoplasty is a

surgical option. Beyond traditional surgery, regenerative stem cell therapies [18] and their combination with cross-linking [5] offer promising avenues for enhancing corneal stability.

While advanced and often costly imaging technologies are available, traditional assessment relied heavily on Placido disc-based corneal topography, which evaluates anterior corneal curvature. This method utilizes reflected concentric rings to generate a color-coded map, enabling detection of irregularities on the anterior corneal surface. Localized anterior corneal steepening is an important early clinical sign of keratoconus that can be detected using this approach. However, Placido-based topography cannot assess posterior corneal elevation or pachymetric distribution, provides limited spatial coverage, and may yield false-positive findings when used as a standalone metric. Therefore, though useful, it should be complemented with other diagnostic approaches to ensure a comprehensive assessment [15]. Other systems include slit scanning systems, Scheimpflug systems, anterior segment optical coherence tomography (AS-OCT) and biomechanical devices focusing on strength or softness of cornea.

Although largely superseded by Scheimpflug imaging and AS-OCT, slit-scanning tomography enabled measurement of anterior and posterior corneal elevation, curvature, and full-thickness pachymetry. In contrast to Placido-disc topography, which evaluates only anterior corneal curvature, corneal tomography and AS-OCT provide three-dimensional assessment of both corneal surfaces and thickness distribution. These tomographic modalities, particularly epithelial and stromal thickness mapping obtained with AS-OCT, are now considered essential for the detection of early and subclinical keratoconus [1] [15] [19].

Comparative studies between various optical imaging platforms and Swept-Source OCT (SS-OCT), such as the Casia SS-1000, demonstrated the latter's capacity for high-resolution 3D corneal reconstruction. Research indicates that SS-OCT measurements yield high repeatability across healthy, post-LASIK, and keratoconus cohorts [20]. Furthermore, significant inter-device agreement was established between Placido-disc, Scheimpflug, and OCT-based topographic measurements [21].

Morphological features, development of the disease, optical signs, and index-based systems can help in determining the severity and development of KC. McMahon and colleagues [22] proposed a severity index score to identify the severity and progression.

Historically, keratoconus (KC) severity was graded using the Amsler-Krumeich (AK) classification, which categorizes the disease into four stages (grades I-IV, with IV being the most severe). This system is based on central anterior corneal curvature, apical corneal thickness, refractive error, and the presence or absence of corneal scarring. A key limitation of the AK classification is its inability to detect early and subclinical KC, which can now be identified using modern corneal imaging technologies. This limitation restricts timely consideration of contemporary treatment options [23].

The Collaborative Longitudinal Evaluation of Keratoconus (CLEK) classification also grades disease severity on a similar ordinal scale. CLEK incorporates average corneal power and the root mean square error (RMSE) of wavefront aberrations derived from Zernike polynomial analysis [24].

More recently, the ABCD classification, enabled by Scheimpflug tomographic imaging, has addressed the limitations of earlier systems. It incorporates anterior and

posterior corneal curvature, thinnest pachymetric location, and distance visual acuity, providing a more comprehensive assessment of KC severity [23, 25].

Placido-disc corneal topography, which evaluates only the anterior corneal curvature, has historically played a central role in the clinical detection of KC and in identifying characteristic anterior surface irregularities [26–28]. However, topography alone is insufficient for the reliable detection of early and subclinical KC, as it does not provide information about posterior corneal elevation or pachymetric distribution.

Computer-assisted analysis of topographic maps has enabled the development of numerous quantitative indices that characterize anterior corneal asymmetry and irregularity associated with KC [10], [11], [29], [30]. The combination of these indices has facilitated the creation of rule-based and algorithmic diagnostic systems that support disease staging and clinical assessment. Well-known examples derived from Placido-based topography include KISA (Keratoconus Percentage Index), KSI (Keratoconus Severity Index), KCI (Klyce/Maeda Keratoconus Index), and KPI (Keratoconus Prediction Index). In contrast, indices such as BAD-D (Belin/Ambrosio Deviation) are derived from Scheimpflug-based tomographic analysis [31]. Comprehensive reviews of these index-based approaches are provided in [32], [15].

In addition to the high incidence of KC in certain regions, the overall numbers would be even higher if subclinical cases could be detected. Early detection of KC is important because treatment becomes more complicated as the disease progresses. Although KC is often asymptomatic at the initial stage, advancements in topographical and tomographic technologies, combined with up-to-date machine learning(ML) algorithms, make early detection possible [33]. It is crucial to recognize KC and monitor its progression, particularly during the normal, subclinical, and forme fruste stages, which are often disputed [34]. Recent advancements in corneal topography and tomography offer the potential for gathering more detailed data. This progress enabled the exploitation of significant developments in ML, resulting in enhanced benefits [15]. Automated screening, diagnosis, and staging for KC require an objective system that maintains credibility. Deep learning algorithms for image processing and classification provide an opportunity with sophisticated features, even for treatment options [34].

In this study, OCT-based epithelial and stromal data and the Ectasia Status Index (ESI) framework introduced by Yousefi and colleagues were focused [35] [36]. The exact mathematical derivation of the ESI remains proprietary; consequently, it is frequently characterized as a black-box model in clinical settings. Recent work demonstrated that this index can be accurately estimated by leveraging Convolutional Neural Network (CNN) architectures trained on raw anterior segment OCT data [37]. Two deep learning methods within a cross-validation framework that leverage sequential clinical data were proposed. One method analyzes single-eye data, while the other integrates bilateral observations recorded on the same date for ESI grade prediction. This approach addresses important gaps in the literature, including the use of multi-site OCT data, bilateral eye integration, and temporal pattern modeling.

2 Literature Review

Early studies employing neural networks for the analysis of corneal maps and keratoconus (KC) detection reported promising results despite relatively small dataset sizes [38], [39]. Accardo and Pensiero [40] differentiated early KC from normal eyes using multiple neural network architectures trained on bilateral parameters derived from Placido-based corneal topography. Vieira and Barbosa compared classical discriminant analysis with a feed-forward artificial neural network using Zernike coefficients extracted from corneal surface data to classify different corneal shape patterns. Later studies began incorporating thickness information derived from OCT. Carvalho and colleagues [41] employed a neural network using stromal and epithelial thickness data to distinguish advanced KC from normal corneas. Similarly, Silverman and colleagues [42] demonstrated that neural network models based on epithelial and stromal thickness profiles could effectively differentiate normal from advanced KC eyes, highlighting localized thinning patterns as strong diagnostic markers.

Machine learning (ML) approaches for keratoconus (KC) detection were investigated by numerous researchers using tomographic data derived from Scheimpflug imaging systems. Muhsin and colleagues [43] analyzed Pentacam data from 644 corneas, each described by 79 tomographic features and labelled across five disease progression stages. Their approach consisted of two phases: initially, random forest, gradient boosting, and decision tree algorithms were employed to construct a derived feature matrix; subsequently, this matrix was used as input for support vector machine (SVM) classification, achieving an accuracy of 99%. In a later study, the same group utilized a consolidated clinical dataset from two eye-care centers in Jordan comprising 1,255 eye observations with the same 79 features [44]. This dataset was categorized into three classes: normal, KC, and asymptomatic KC. The authors applied ANOVA statistical testing to identify the most discriminative features and evaluated multiple classifiers, including k-nearest neighbors (KNN), gradient boosting, decision trees, logistic regression, linear discriminant analysis, Naive Bayes, random forest, and SVM. Among these, the random forest classifier achieved the highest performance with 99.6% accuracy, while gradient boosting and decision trees demonstrated comparable results. Subramanian and colleagues [45] compared multilayer perceptron (MLP), radial basis function neural networks (RBFNN), decision trees, and convolutional neural networks (CNN) using Pentacam tomographic data for KC diagnosis. Mustapha and colleagues [46] evaluated random forest, SVM, and XGBoost based on numerical tomographic indices, whereas Sandhiya and colleagues [47] assessed KNN, SVM, decision trees, and MLP on clinical patient datasets, highlighting the gradual transition of ML-based KC detection from experimental research toward clinical validation.

With the introduction of slit-scanning (Orbscan) and Scheimpflug imaging systems, researchers incorporated corneal elevation and pachymetry data into ML models. Souza and colleagues evaluated the effectiveness of support vector machines, multilayer perceptrons, and radial basis function neural network models to detect KC by using data gathered from Orbscan II maps [48]. Unlike Placido-based topography, Orbscan II provides anterior and posterior elevation maps in addition to full-thickness

pachymetry, enabling the use of three-dimensional corneal descriptors in ML analysis. Their study reported comparable performance across all three ML techniques for distinguishing normal from KC eyes.

Smadja and colleagues reported that their automated decision tree classifiers attained 93.6% sensitivity and 97.2% specificity while distinguishing normal versus FFKC (Forme-Fruste KC) eyes [49]. Cao and colleagues achieved a lower sensitivity and specificity with decision trees [50].

The transition from Placido-based topography to tomographic imaging and OCT substantially enhanced the capability to detect early and subclinical keratoconus. Shi and colleagues combined Scheimpflug tomographic data with optical coherence tomography (OCT) imaging from 121 eyes to train a neural network classifier for distinguishing forme fruste keratoconus (FFKC) from normal eyes. They reported that epithelial thickness features extracted from OCT images were the most discriminative parameters between these groups [51]. Issarti and colleagues proposed a computer-aided diagnosis approach based exclusively on tomographic variables, namely corneal elevation and minimum pachymetry, to differentiate normal from FFKC eyes. Their method first reduced the dimensionality and complexity of the corneal maps using a specially designed mathematical transformation. A feed-forward neural network was then trained on a dataset of 851 eyes, including bilateral normal corneas, FFKC eyes (with clinically confirmed KC in the fellow eye), and mild-to-moderate KC eyes [52]. Finally, Yang and colleagues employed a two-step decision tree model for KC detection using parameters derived from OCT-based corneal and epithelial thickness maps and their spatial patterns [1].

Deep learning approaches using corneal maps as images gained popularity. Lavric and colleagues used an image dataset to develop an algorithm with 1,500 images of healthy eyes and 1,500 images of KC eyes. Further, the model was trained using a Convolutional Neural Network (CNN) with 1,350 images and tested on 400 equally distributed eye images. The authors reported an accuracy of 99.33% [53]. Later, the same group experimented with corneal parameters, including elevation, topography, and pachymetry, to detect KC severity. The dataset consisted of 2,881 patients and 5,881 eyes from Brazil, acquired with a Pentacam Scheimpflug instrument. They utilized traditional ML algorithms with various configurations following a feature selection algorithm [54]. Kamiya and colleagues [55] utilized anterior/posterior elevation and curvature, total refractive power, and pachymetry maps gathered from anterior segment optical coherence tomography for a ResNet-18 model. They applied six neural network models to each of the six color-coded maps and computed the arithmetic mean of their outputs; this approach achieved an accuracy of 99.1%, a sensitivity of 100%, and a specificity of 98.4% in distinguishing KC eyes from normal eyes. The model also resulted in an accuracy of 87.4% for disease staging using the Amsler-Krumeich classification. Similarly, Chen and colleagues [56] trained VGG-16 models using axial, anterior/posterior elevation, and pachymetry maps collected from a Scheimpflug imaging device. They detected normal versus KC eyes with 97.85% accuracy using concatenated maps. The model also classified KC stages with 90% accuracy between stages 1 and 2, and 85.37% between stages 2 and 3. Xie and colleagues targeted the screening of patients prior to refractive surgery to eliminate those

with vulnerable corneas; they updated only the weights of the fully connected layers while keeping other weights pre-trained on ImageNet. Their dataset contained 6,465 Pentacam HR images from 1,385 patients, including normal, suspect, and postoperative myopic groups; however, they achieved lower sensitivity in classifying FFKC compared to other groups [57]. In a study by Kuo and colleagues, three CNN models such as VGG16, InceptionV3, and ResNet152 were adopted for transfer learning. All models yielded sensitivity and specificity values over 90%, with ResNet152 attaining 97% specificity. While clinically diagnosed KC was easily categorized, FFKC diagnostic accuracy remained significantly below adequate levels [58].

Recent studies have increasingly explored the use of raw tomographic data and multimodal inputs for keratoconus detection. Xu and colleagues proposed an evaluation framework based on tomographic parameters derived from Scheimpflug imaging [59]. Subsequently, Feng and colleagues introduced a deep learning approach (KerNet) that directly utilized raw Pentacam data for the detection of keratoconus and subclinical keratoconus without relying on precomputed indices [60]. Mirsalehi and colleagues proposed a CNN-based screening predictor for early KC detection [37], while Al-Timemy and colleagues evaluated CNN, Xception, and InceptionResNetV2 architectures using two independent datasets acquired from Scheimpflug devices [61]. Other CNN-based KC detection frameworks incorporating transformer-based and hybrid architectures have also been applied to tomographic videos and corneal biomechanical data, as reported in the literature [62], [63], [64], [65]. Notably, the studies by Al-Timemy and colleagues and Mirsalehi and colleagues emphasized cross-dataset validation and the prediction of disease progression prior to significant visual deterioration.

ML algorithms for KC were surveyed in various studies, such as [66], [67], [45], [46], and [68]. Many ML studies were tested only on limited data and require more rigorous validation and standardized approaches [45], [68].

Most of the studies discussed above employed supervised learning approaches that rely on labelled input data. In contrast, Yousefi and colleagues [36] applied an unsupervised machine learning framework to identify keratoconus (KC) patterns directly from SS-OCT data without predefined class labels. Their method combined dimensionality reduction with density-based clustering to reveal four distinct groups corresponding to different stages of disease progression.

To objectively evaluate the clinical relevance of the derived clusters, the results were compared with the CASIA Ectasia Status Index (ESI) [69]. The first cluster predominantly contained normal eyes, the second consisted mainly of normal and forme fruste keratoconus (FFKC) eyes, the third included mostly mild KC, and the fourth comprised largely advanced KC eyes. Although the clustering showed good agreement with ESI grading, the approach did not yield a clearly separable cluster exclusively representing FFKC eyes.

Building upon this limitation, the present study proposes a deep learning approach based on the long short-term memory (LSTM) architecture, a specialized form of recurrent neural network (RNN) designed to model temporal dependencies in sequential data. Unlike conventional feedforward networks, LSTMs incorporate memory cells and gating mechanisms that enable the retention of information over time. This

property makes LSTMs particularly well suited for analyzing longitudinal clinical measurements, which form the basis of the time-series data used in this study [70].

3 Overview of the Dataset

A sizeable dataset of corneal optical coherence tomography (OCT) images from SS-1000 CASIA OCT imaging systems was collected across several sites in Japan. This dataset included 12,424 observations of 3,162 eyes, characterized by 482 features, including temporal (date) information for each observation.

SS-OCT derives all corneal parameters from tomographic imaging. Unlike Placido-based systems that measure surface topography from reflected rings, SS-OCT reconstructs the three-dimensional geometry of the cornea and computes curvature and asymmetry indices from the reconstructed anterior and posterior surfaces. The parameters obtained from SS-OCT can be grouped into elevation-based (e.g., anterior and posterior elevation), thickness-based (e.g., total, epithelial, and stromal thickness), curvature-based (e.g., Steepest.1, Axial K), and asymmetry-based indices derived from the anterior curvature map. For example, Steepest.1 represents the maximum localized anterior curvature and indicates the magnitude and location of the cone apex, whereas Asymmetry.5 quantifies anterior curvature asymmetry within the analysed central zone, reflecting cone decentration and irregular astigmatism. CV_P.4mm gives the posterior corneal curvature variability parameter computed over the central 4-mm zone.

The progression status of each eye was represented by the Ectasia Status Index (ESI), which ranges from 0 to 100, where higher scores indicate greater severity. For this study, three screening labels were extracted based on ESI values: eyes with an ESI between 0 and 4 were classified as healthy, while those with an ESI of 30 or higher were categorized as KC. Eyes falling between these ranges were assigned as Forme Fruste KC (or keratoconus suspect). In keratoconus diagnosis, the Belin-Ambrosio (BA) index and the ESI were validated as effective instrument-based screening tools [36].

In this study, a publicly available dataset [35, 36] was used; the cited data is accessible via the GitHub repository[1]. This dataset contains the diagnosis dates for each patient alongside eye-side information. The features according to their importance scores were ranked and implemented two distinct LSTM-based approaches.

While previous researchers [36] utilized and cited this publicly shared data, the original article did not involve new studies on human or animal participants. The masked dataset was already ethically approved and available [35]. The analysis of the dataset and the methodology using the dataset are described in Section 4 and Section 5.

4 Analysis of the Dataset

4.1 Males and Females Groups

The original dataset has 12,424 observations across 3,162 eyes, featuring 482 distinct variables. To ensure data integrity, the dataset was refined by selecting only the final

[1] https://github.com/DM2LL/Cornea

measurement for cases where multiple observations were recorded for the same eye on a single day. This filtering process resulted in a final cohort of 8,282 observations from 1,796 participants.

The decision to take the final daily measurement was driven by the high variance observed in ESI values within same-day recordings. As illustrated in Figure 1, the standard deviation distribution of same-day observations confirms significant fluctuations. By selecting the final value, which represents the definitive output retrieved from the device with minimized noise avoids the statistical bias of including redundant, fluctuating data points.

The processed dataset reflects a mean age of 70.1 ± 14.9 years and a mean ESI of 21.2 ± 28.0. The gender distribution consists of 4,803 female and 3,479 male observations (Figure 2). Despite the smaller sample size in the male cohort, this group exhibited a higher mean ESI. This disparity is partially attributed to the distribution of healthy labels; specifically, a higher proportion of the female group (42.3%) was labelled as healthy compared to the male group (39.8%).

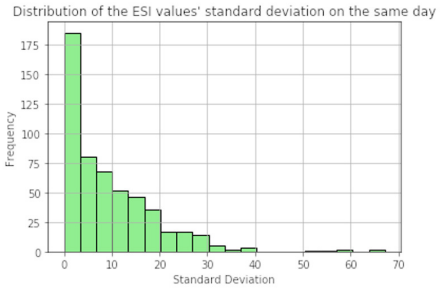


Fig. 1 Standard deviation distribution of the ESI values for the dates where the patients have more than one observation recorded

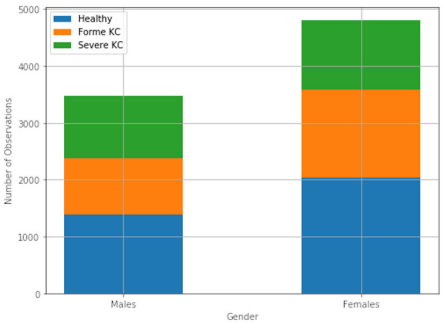


Fig. 2 Number of observations recorded for males and females. Blue block shows observations labelled as Healthy with the ESI system. Orange and green blocks correspond to Form KC and KC labels, respectively.

4.2 Age and ESI

The analysis categorized the cohort into six distinct age groups, with detailed characteristics and mean ESI values summarized in Table 1. As shown in Figure 3, the dataset is predominantly composed of older adults, with 6,983 observations(1483 participants) attributed to individuals aged 60 and over. Furthermore, Figure 4 illustrates the distribution of ESI values across these groups. The data reveals a bimodal trend, indicating that the majority of eyes exhibit either notably low or high ESI values, with fewer observations falling in the intermediate range.

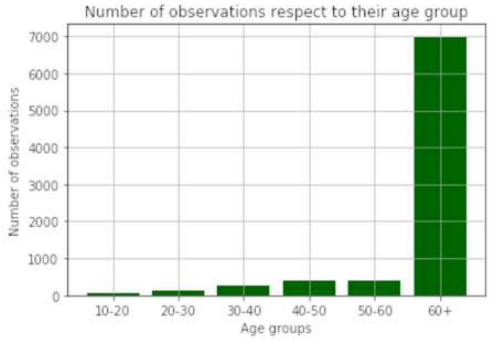


Fig. 3 # of observations belonging to six separate age group

Table 1 Detailed information about age groups and their mean ESI values.

Age	**10-20**	**20-30**	**30-40**	**40-50**	**50-60**	**60+**
# of participants	23	43	64	88	95	1483
Mean ESI	37.3 ± 38.1	29.2 ± 36.6	40.04 ± 36.2	35.2 ± 37.8	20.1 ± 29.9	19.6 ± 26.3

4.3 Left eyes and Right Eyes

The dataset includes observations from both left and right eyes and is well-balanced in terms of sample size for each, as shown in Figure 5. Despite this balance, the mean ESI for left eyes (20.6 ± 27.4) is slightly lower than that of right eyes (21.9 ± 29.0). As illustrated in Figure 5, the right eye cohort exhibits a higher frequency of elevated ESI values (≥ 30), which accounts for this higher mean.

A significant portion of the cohort includes bilateral data: 1,602 individuals have at least one observation for both eyes, 539 have at least two observations per eye, and 333 have at least three. This relationship between observation frequency and participant count is detailed in Figure 6.

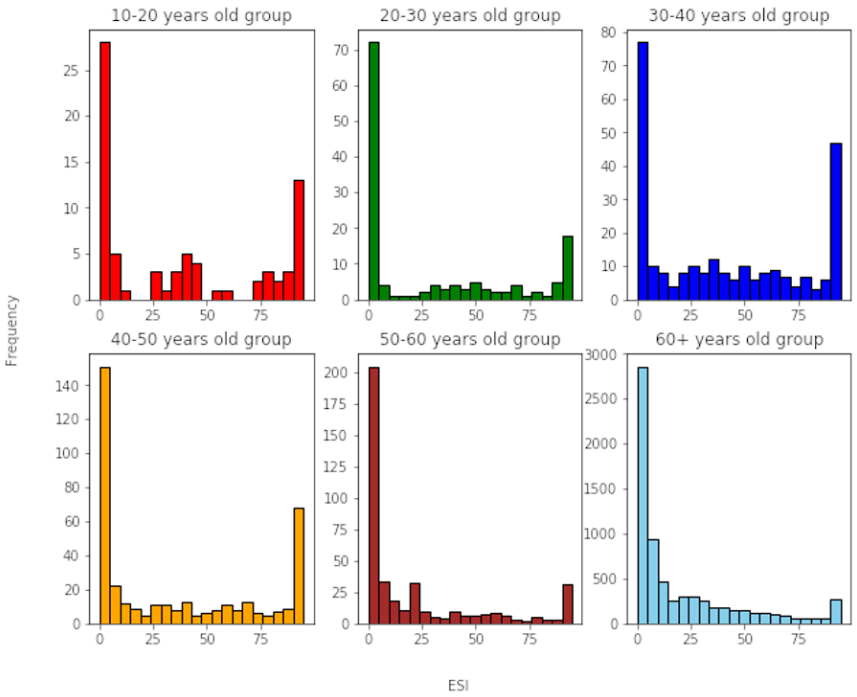


Fig. 4 Distribution of the ESI value with respect to the age groups.

Figure 7 highlights the intra-individual differences between the mean ESI of the left and right eyes. For participants with at least two observations per eye, the left eye generally exhibits a lower mean ESI than the right. However, as the threshold for the required number of observations increases, this trend shifts to favor the left eye. This suggests that in patients with high longitudinal engagement (multiple screenings), the left eye often presents in a more severe condition relative to the right.

Finally, Figure 8 presents the Root Mean Square Error (RMSE) values across various contexts. Here, "minimum observations" refers to the threshold of screenings required for patient inclusion. While most RMSE values stabilize as the minimum number of observations rises, the Right Eye Max RMSE and Patient-based Mean RMSE decrease significantly. Conversely, the Left Eye Max RMSE increases in correlation with the number of observations, further supporting the observation of increased severity or variability in the left eyes of frequently monitored patients.

4.4 Number of observations vs ESI for eyes

The number of observations recorded for an eye is typically small, with many eyes having fewer than three observations, as illustrated in Figure 9. The relationship between an eye's mean ESI and the number of observations conducted for that eye can be observed in Figure 10. This graph indicates that eyes with a higher number of observations tend to have a greater mean ESI compared to those with fewer observations, suggesting that eyes with elevated ESI values are monitored more frequently.

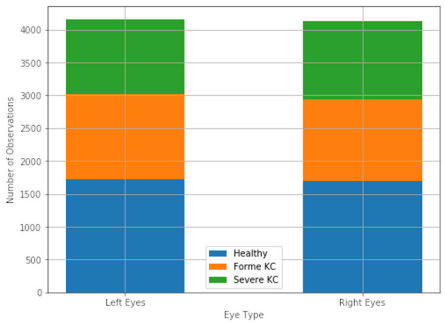


Fig. 5 Number of observations recorded for left eyes and right eyes. Blue: observations labelled as Healthy with the ESI system. Orange: and green blocks correspond to Forme KC and KC labels respectively.

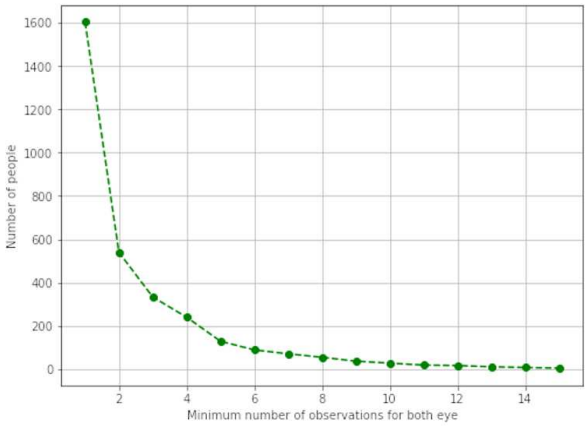


Fig. 6 Number of patients that have observations recorded for both their left eye and right eye.

Notably, the mean ESI value peaks for eyes that have 15 observations; however, beyond this point, the mean ESI value decreases as the number of observations continues to increase. This trend may be attributed to more frequent visits by recovering patients.

As illustrated in Figure 9, the number of observations recorded per eye is relatively low, with the majority of eyes having fewer than three observations. The relationship between an eye's mean ESI and its total number of observations is shown in Figure 10. The data indicates a positive correlation between monitoring frequency and ESI values, suggesting that eyes with elevated ESI are subject to more frequent clinical observation. Notably, the mean ESI reaches its peak in eyes with 15 recorded observations. Beyond this threshold, however, the mean ESI begins to decline despite further increases in the number of screenings. This inversion in the trend may be attributed to a "recovery phase" effect, where patients with the highest volume of visits are undergoing successful treatment or monitoring during a period of clinical improvement.

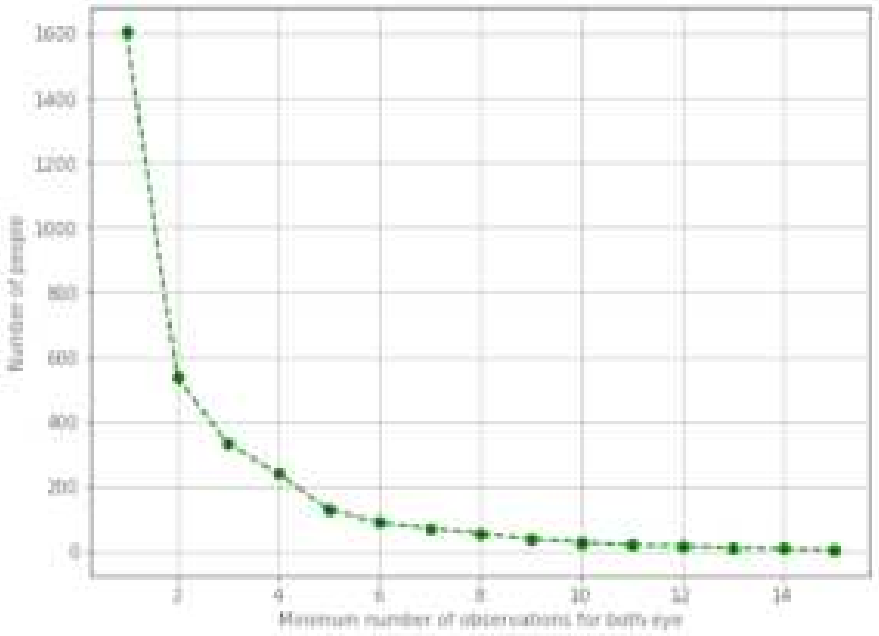


Fig. 7 The relation of the left eyes' ESI and right eyes' ESI for the patients that have observations recorded for both their eyes

4.5 Posterior ESI vs Anterior ESI

The ESI value of an eye is determined by two indices: Posterior ESI and Anterior ESI, with the final ESI defined as the maximum value of the two. Analysis of the intra-observation differences between these indices reveals a mean difference of 4.35 ± 21.4. This positive mean indicates that the Posterior ESI is generally higher than the Anterior ESI, making it the primary determinant of the final ESI value in the majority of cases. However, the high standard deviation relative to the mean suggests substantial variability in the relationship between these two indices across the dataset. Figure 11 illustrates the distribution of these ESI differences by age group, providing further insight into how the dominance of posterior versus anterior values may shift across different demographics.

4.6 Correlation results – Change in correlations between groups

A correlation heatmap illustrating the relationship between individual features and the ESI value is presented in Figure 12. The variables exhibiting the strongest positive correlations with ESI include Score.Anterior, Asymmetry.1, Asy..Keratometric, Asymmetry.3, and SAI. Conversely, K.Max..10mm..1 and K.Max..8mm..1 have significant negative correlations. This inverse relationship indicates that higher values in these specific keratometric parameters are associated with lower ESI values. These

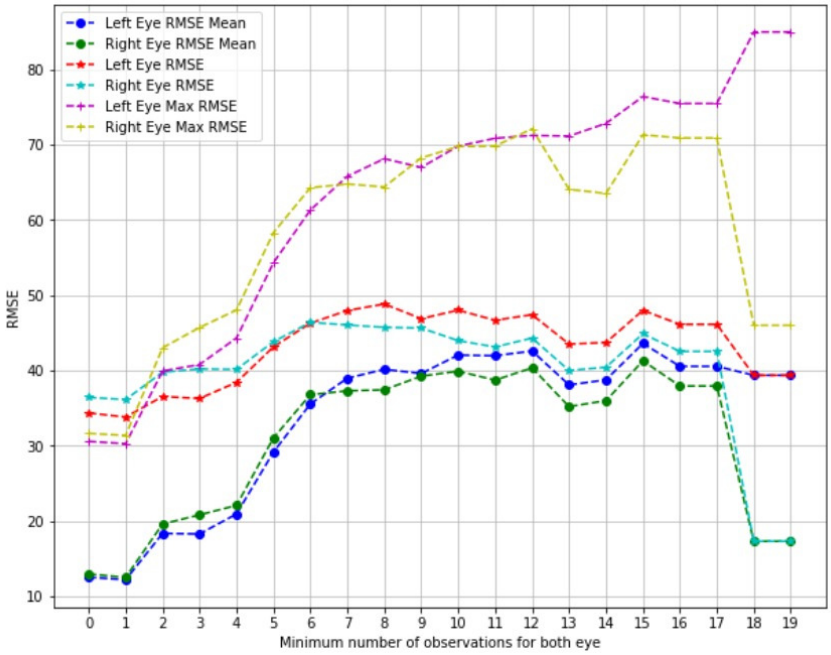


Fig. 8 RMSE vs. minimum number of observations

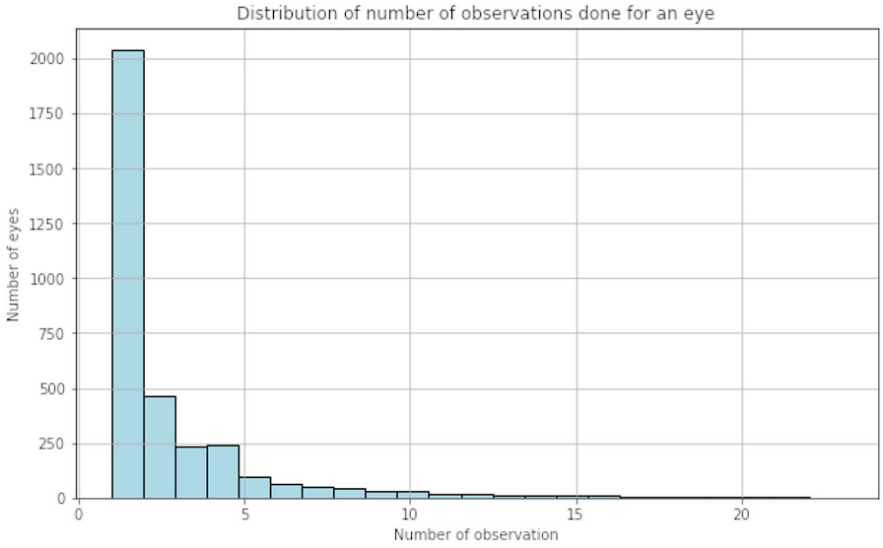


Fig. 9 Relation of the number of observations recorded for each eye. Many eyes have less than 3 observations.

findings suggest that while anterior asymmetry markers are positively linked to ESI, these maximal curvature measures move in the opposite direction.

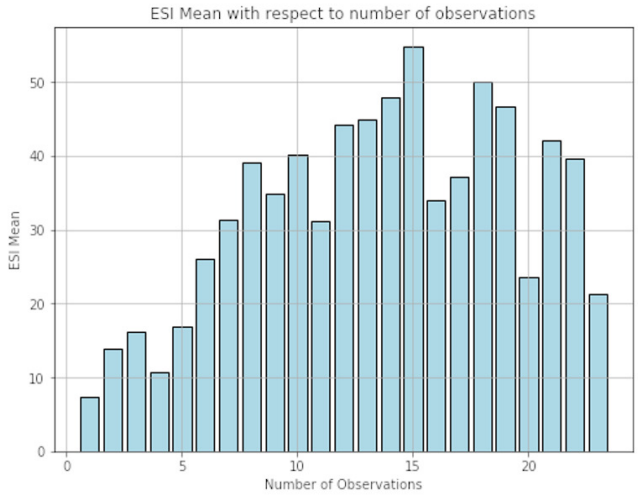


Fig. 10 Number of observations done for eyes and their mean ESI value. Maximum mean ESI is for the eyes' that have 15 observations recorded.

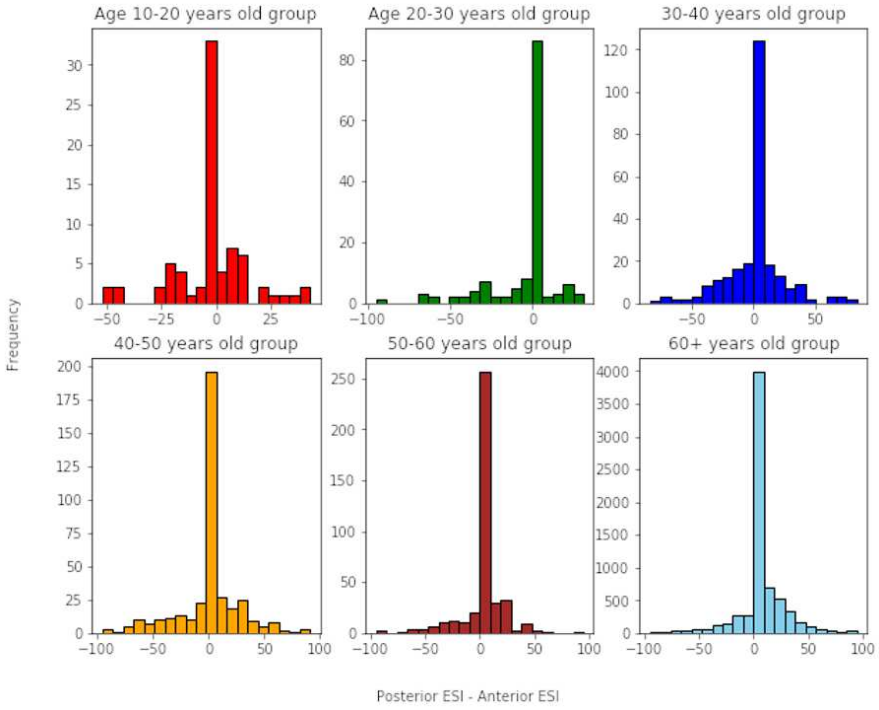


Fig. 11 Distribution of the value difference between Posterior ESI and Anterior ESI seperated by six age groups.

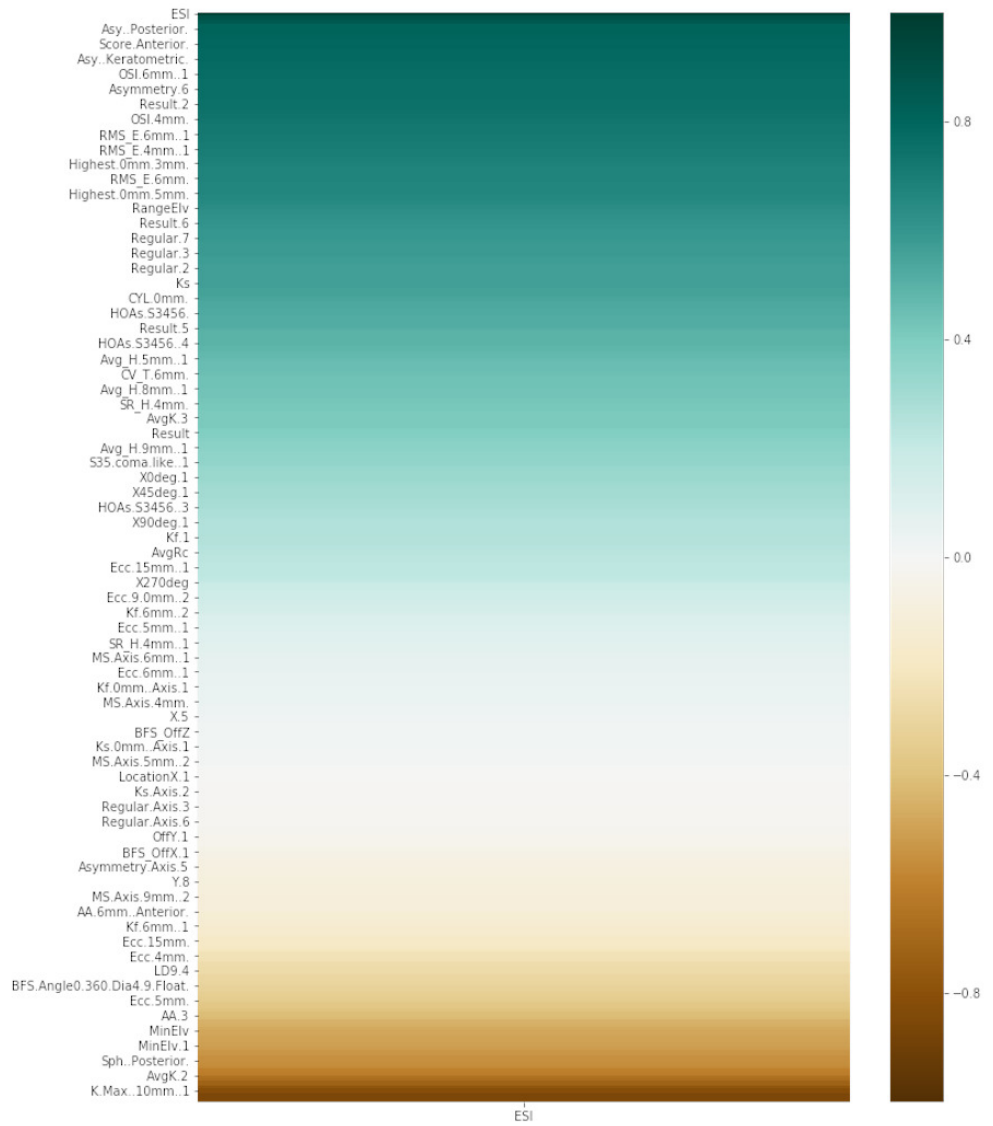


Fig. 12 Heatmap of the correlation matrix of the features to the ESI.

4.7 Evaluation of Eyes with Changed Group Classification

The ESI system categorizes disease severity using specific diagnostic thresholds: an ESI $\geq$ 30 indicates Keratoconus (KC), while values between 5 and 29 are classified as Forme Fruste Keratoconus. Understanding the temporal and observational requirements for an eye to cross these thresholds is critical for clinical monitoring. By analyzing longitudinal trends, the average time (days) and the number of clinical encounters (observations) necessary for an eye to transition between these diagnostic

categories were calculated. The results of these transitions are summarized in Table 2. A total of 174 eyes progressed to the KC classification ($ESI \geq 30$), requiring an average of 164.0 days and 1.89 observations. In contrast, 181 eyes that initially presented with KC saw their ESI values regress to below 30. This downward transition took significantly longer, averaging 174.9 days and requiring 2.45 observations. These findings suggest an asymmetry in disease dynamics: ESI values in this cohort tend to increase rapidly during progression but decrease more gradually during periods of clinical improvement.

Table 2: Number of observations and days required for an eye to change labels

	Healthy to Forme KC	**Forme KC-to-Healthy**	**Healthy-to-KC**	**KC-to-Healthy**	**Forme KC-to-KC**	**KC-to-Forme KC**	**KC-to-Not KC**	**Not KC-toKC**
# of Obs.	1051	964	292	228	1550	1600	1657	1634
# of Eye	179	174	37	31	159	173	174	181
Avg. Days Required	143.1	147	196.9	239	160.7	177.8	164	174.9
Avg. Obs. Required	1.6	1.58	1.89	3.2	1.88	2.56	1.89	2.45

The original dataset contained a missing entries with NA values, which precluded direct analysis by the proposed models. To ensure data robustness, a feature-level filtering threshold was applied: any column containing at least 3,000 missing values was excluded from the study. The specific features removed during this process, along with their respective missing value counts, are detailed in Figure 13. In addition to sparsity-based filtering, variables unrelated to clinical ocular characteristics were removed. These included administrative data from the optical device and the constituent indices used to derive the final ESI value namely Posterior ESI, Anterior ESI, and ESI Status. These latter features were removed to prevent data leakage, as they are mathematically redundant with the target ESI variable.

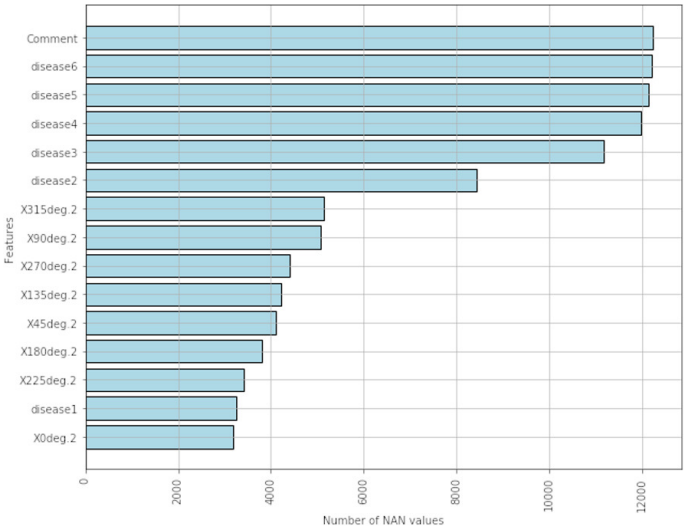


Fig. 13 Features that have more than 3000 NaN values. These features are dropped in the preprocess.

5 Methodology

In the methodology, two models were proposed. The one-eye model considers each eye as an independent sequence. The double-eye model considers both eyes of an patient. The data was cross-validated by benefiting from the sequence analysis. Depending on the model, the primary units of analysis, either individual eyes or individual patients, were split into training and test cohorts. The data from each eye are split so that all observations from a single eye appear entirely in either the training or test set, the same eye's data is not present in both to help avoiding data leakage and ensure a fair assessment. For the double-eye model, all observations from both eyes of a single patient are grouped together. This means that the left and right eye data from any given patient will be assigned to either the training or the test set, but never split between the two.

Following the removal of sparse and administrative columns, the dataset was refined from an initial 12,242 observations with 482 features to a final set of 9,549 observations with 435 features. To eliminate scale-related distortions, all features were scaled to a range of $[0, 1]$ using Min-Max normalization.

The feature importance was assessed by using the f_regression function [2] from the Scikit-learn library, which ranks variables based on their F-test scores. Feature selection was implemented for two primary reasons: (1) to decrease training time, and (2) to overcome overfitting by reducing noise in the data by eliminating the unrelated features. The top 50 prioritized features are detailed in Table A1 in the Appendix.

[2] https://scikit-learn.org/stable/modules/generated/sklearn.feature_selection.f_regression.html

5.1 One-Eye Model

In case of multiple observations on the same day, after eliminating duplicate instances and instances with NA values, only the most recent observation of each eye was retained, and the others were discarded. Initially, a total of 9549 observations from 3398 eyes (1796 patients) were recorded for each eye. The observations for each eye were sorted according to their date. On average, there are 2.44 ± 2.84 observations per eye. Due to irregular observation dates, new observations in the training dataset were introduced through linear interpolation. Given two successive measurements, an artificial line was created by populating a data point for each month to represent that month. As a result, the number of observations for each eye was populated, and the time between consecutive observations became constant from the first measurement date to the last measurement date. The input data for the one-eye model comprised observations from 3398 eyes with 256 features, leading to 8274 eye observations in total.

The model consists of three layers. The first layer is an LSTM layer with 256 neurons with tanh activation function that returns all the hidden states of each time step. The second layer contains 128 densely connected neurons, with the ReLU function serving as the activation function for these neurons' outputs. The final layer consists of a single neuron connected to the previous layer, which outputs the predicted ESI value based on the input observations. The mean square error was employed as the loss function, and the Adam optimizer was selected as the gradient optimizer. The learning rate was reduced by a factor of 0.5 during the training when the loss measurement reaches a plateau. The batch size was set to 32, and the number of epochs was set to 75. During the training, the model cross-validated the training data 10 times to assess its performance, using 90% of the data for training and 10% for testing at each cross-validation step.

The data was cross-validated using the Clasp algorithm [71], [72], which identifies closed frequent sequences. A sequence is defined as a series of events or items that occur frequently within a data set. Due to its anti-monotonic property, no superset of a closed frequent sequence exists with the same frequency. With the virtue of closed frequent sequences, the frequent sequences were compressed. The ESI score is used and it is further partitioned into five labelled intervals such that each observation of an individual belongs to one of the five intervals. This enables transforming the dataset into five transactions that contain the labels. Each transaction entry is an individual having a label in the course of time.

The transactions were generated as follows. An ESI score between 0 and 4 is mapped to normal, and it will be only in one interval. It is represented as grade 0, and its label value is 1. The FFKC score takes values between 5 and 29, and it was assigned 5 interval labels from 2 to 6. Finally, KC can take a value from 30 to 100; and accordingly, it has 14 possible interval labels from 7 to 20. Subsequently, the entire dataset was transformed into a matrix with 20 columns, and each observation of an individual is labelled according to the interval number it belongs to. Then, the existing timestamp of an individual is also considered, and all the closed sequences are extracted.

A new dataset was constructed with eyes as rows and closed sequences as columns. Each row (eye) contains the number of occurrences in each corresponding column. Next, the k-medoids clustering algorithm [73] with $k = 10$ was applied, This was used for dealing with outliers and noise. Based on the identified clusters and the sequential behaviour, individuals (eyes) were categorized under the same groups. Stratified sampling was utilized based on the cluster sizes to ensure that sequences are used in a balanced manner; this in combination with feature selection reduced the risk of overfitting. Both the training and testing phases of the experiments employed similar sizes and sequences.

5.2 Double-Eye Model

The double eye model utilizes data from both eyes of patients simultaneously. It takes as input sequential data that combines the observations from both eyes. Instead of treating the left and right eyes separately as one observation like the one-eye model, both eyes together were utilized to predict their ESI values. To ensure the model's effectiveness, only patients with a minimum of two observations for both eyes were included. To further prepare the input for the model, the data was interpolated in the same way followed for the one-eye model. This was performed for two primary reasons. First, many patients did not meet the minimum requirement of two observations per eye at once, and this resulted in a significant reduction in the available data. Second, it is required to create reasonable number of input points, eventually, observations from the left and right eyes of the same patient recorded on the same day. The observations of the left eye and right eye recorded on the same day were merged. When the examination dates do not match, the instance values were interpolated by using the dates of the observation points of both eyes. Ultimately, the data from both eyes for each date in this interval were combined, resulting in 539 individuals (patients) having observations with 430 features for each eye, leading to 11632 individuals in total.

The architecture of the double-eye model is similar to that of the one-eye model; each consists of three layers. The first layer contains 256 LSTM neurons with tanh activation function returning sequential information from the previous state, while the second layer features 128 densely connected neurons corresponding to each LSTM neuron. ReLU functions were chosen as the activation function for the neurons in the second layer. The last layer consists of two neurons which predict the ESI values for the left and right eyes, respectively. Mean square error was used as the loss function, and the Adam optimizer was selected for gradient optimization. The learning rate was halved when the loss value reached a plateau. The batch size and number of epochs were set to 32 and 2400, respectively. Similar to the one-eye model, the data was cross validated ten times to evaluate the performance of the model.

The double-eye model was cross-validated after merging the left and right eyes . By following the same approach as in the one-eye model, instead of eyes, patients were split in the same way. The difference is that the merged eye observations will have two different labels coming separately from the left and right eyes during the closed sequence extraction stage. The right eye and the left eye affiliation were also added to

the label information to underline each label's belongingness. For example, an observation at a specific date will have (L1 R3) to represent the case where the L(eft) eye belongs to interval label 1 and the R(ight) eye belongs to interval label 3. Thus, due to the nature of the dataset, closed sequences were obtained by particularly differentiating the labels of the left eye and the right eye sequences. Clasp algorithm [71], [72], identifies closed frequent sequences. These closed sequences are the columns and each row holds a patient. For each closed sequence, the corresponding number of occurrence in patient's data is held. k-medoids clustering algorithm [73] with $k = 10$ was applied to partition the patients. Thus, stratified sampling was performed based on the cluster sizes. Both the training and testing phases of the experiments employed similar sizes and sequences.

6 Discussions and results

Assessments of the anterior and posterior corneal surfaces contribute to diagnosis. For the anterior cornea, the evaluation retrieves information regarding the spherical, asymmetry, and regular astigmatism components through Fourier analysis. For the posterior cornea, the steepest point of instantaneous power, along with asymmetry, regular, and higher-order irregular astigmatism components from Fourier analysis, are used to estimate the ESI result [37]. In addition to the steepening information, some contributing features focus on posterior asymmetry, variables that start with Kmax, DSI, CSI, SAI, OSI, and CV_P, SDP with varying region of interests (see Table A1).

Kmax refers to the maximum axial or sagittal curvature on the corneal curvature map. It is used for screening ectatic progression. It was detected that Posterior asymmetry, including the corneal surface shape surpassing basic curvature measurements, was significantly greater when KC eyes had no topographic changes appearing on the corneal map [74]. Although standard anterior keratometry may show no significant difference between normal and FFKC eyes, steepest posterior keratometry was found to be significantly different in FFKC and KC eyes, specifically showing inferior decentration and altered curvature values compared to normal eyes [19].

DSI (The Differential Sector Index) is the difference between boundary refractive powers. Opposite Sector Index (OSI) is the difference between the maximum refractive power and the refractive power at its opposite side. CSI (Center Surround) is the difference between the refractive powers of the outer region and the centre region. SAI (Surface asymmetry index) is relevant to the alterations in corneal symmetry. SDP (Standard Deviation Power) represents the intrapatient asymmetry. CV_P is used to give the variation coefficient of refractive power.

The OSI and DSI represent abnormal local cones in the outer areas, whereas CSI focuses on abnormal central cones. It was reported that SAI serves as a marker for keratoconus progression, emphasizing irregular astigmatism and decentered cones. SDP is relevant to corneal asymmetry [26]; and CV_P is indicative of worsening stages of KC [75].

The confusion matrix for the one-eye model (Table 3) indicates that 3529 eye observations were correctly classified as healthy (98.6%). However, healthy eyes were primarily misclassified as FFKC in 46 instances, and only one eye observation was

Table 3 Aggregate results of the test data predictions for each cross-validation step in the one eye model

	Healthy Predicted	Forme Fruste Predicted	KC Predicted
Healthy Real	3529	46	1
Forme Fruste KC	195	2141	39
KC Real	1	59	2263

incorrectly classified as KC. A total of 2141 FFKC eye observations were classified correctly (90%). Eyes labelled as FFKC may also be misidentified as healthy in 195 cases and as KC in 39 instances. Additionally, 2263 eye observations were accurately classified as KC (97.4%), while some KC observations were misclassified as FFKC in 59 instances and as healthy in one instance. Overall, the model accurately predicted 7933 out of 8274 observations (95.8%).

Table 4 Aggregate results of the test data predictions for each cross-validation step in the double-eye model

	Healthy Predicted	Forme Fruste Predicted	KC Predicted
Healthy Real	4638	156	1
Forme Fruste KC	143	3376	142
KC Real	1	92	3083

The confusion matrix (Table 5) for the double-eye model illustrates that 4622 healthy eye observations were classified correctly. Healthy eye observations were only misclassified as FFKC(171). A total of 3376 FFKC eye observations were classified correctly. FFKC eyes were misclassified as 143 healthy and 142 KC. Out of 3176 KC eye instantances, 92 instances were predicted as FFKC, and one of the observations was classified as healthy.

The double-eye model predicted the ESI values of both eyes from each partition obtained through cross-validation. The validation set was interpolated in the same manner as the training set, as there were insufficient real data points for testing. The average RMSE value calculated for the model was 3.38. After predicting the ESI values from the sequential data fed into the double-eye model, all ESI values were labelled, Out of 4795 healthy observations, 4638 were classified correctly (96.7%). Closer to the one-eye model, the double-eye model achieved almost 100% accuracy in accurately distinguishing healthy and KC eyes. Out of 3176 observations, the double-eye model correctly classified 3083 (97%). Predicting observations labelled as FFKC proved challenging, 3376 out of 3661 observations were classified correctly (92.2%). Overall, the double-eye model correctly predicted 10583 out of 11632 observations (95.4%).

The same dataset prepared for the double eye model was split for the use with the one eye model.The confusion matrix (see Table 5) reports that 4622 healthy eye observations were classified correctly. Healthy eye observations were misclassified as

Table 5 Aggregate results of the test data predictions for each cross-validation step in the one eye model after transforming the dataset in to the double-eye model

	Healthy Predicted	Forme Fruste Predicted	KC Predicted
Healthy Real	4622	171	2
Forme Fruste KC	152	3362	147
KC Real	3	127	3046

FFKC (171) and KC (2). A total of 3362 FFKC eye observations were classified correctly. FFKC eyes were misclassified as 152 healthy and 147 KC. Out of 3176 KC eye instances, 127 instances were predicted as FFKC, and three of the observations were classified as healthy.

The one-eye model predicted the ESI values of both eyes from each partition obtained through cross-validation. The validation set was interpolated in the same manner as the training set, as there were insufficient real data points for testing. The average RMSE value calculated for the model was 3.54; the results are reported in the matrix shown in Table 5. Out of 4795 healthy observations, 4622 were classified correctly (96.4%). Similar to the double-eye model, it achieved almost 100% accuracy in distinguishing healthy and KC eyes. Out of 3176 observations, the one-eye model using the dataset in the double -eye model correctly classified 3046 (95.9%). This model also successfully separated observations labelled as KC from those labelled as healthy with nearly 100% accuracy. Predicting observations labelled as fruste forme KC proved challenging, 3362 out of 3661 observations were classified correctly (91.8%). Overall, the double-eye model correctly predicted 11030 out of 11632 observations (94.8%).

Two models were proposed and achieve high accuracy in classifying eyes into three groups. They predict the ESI value by considering past observations and topographic results. The one-eye model achieved an overall accuracy of 95.8% and successfully separated KC and healthy labelled eyes with 100% accuracy. The double-eye model was proposed in order to reveal the latent relationships between the observations of both eyes This approach used dataset obtained by merging both eye observations examined at the same time for the same patient. This dataset was also fed into the one-eye model after splitting the left and right eyes. The double-eye model had 95.4% correctly predicted observations. The same dataset for the one-eye model had slightly lower correct prediction ratio of 94.8%. These results imply that assessing both eyes at the same time in KC can provide valuable information for predicting disease severity. Many corneal conditions, such as KC, often affect both eyes, although the severity may differ between them.

7 Conclusions and Future Work

This study investigated the prediction of keratoconus (KC) severity progression using the ESI and machine learning-based approaches. An existing dataset enriched with corresponding severity scores was analyzed, and Long Short-Term Memory (LSTM)

networks were employed to predict disease stages based on sequential corneal measurements and topographic characteristics. Two different modeling strategies were evaluated: an eye-based approach, where each eye was considered an independent sample, and a patient-based approach, where bilateral eye information was incorporated to capture potential inter-eye relationships. The findings demonstrated that advanced machine learning techniques can effectively support KC severity assessment and provide valuable insights for early diagnosis and disease monitoring.

The proposed models achieved high classification performance in distinguishing healthy, forme fruste keratoconus (FFKC), and KC cases that highlightsw the importance of integrating anterior and posterior corneal parameters, asymmetry indices, and irregularity-related features. The results indicate that incorporating information from both eyes may provide additional clinical value by capturing latent relationships associated with disease progression. Although early-stage KC detection, particularly in FFKC cases, remains challenging due to subtle corneal changes, machine learning approaches offer effective avenues to cope with the limitations of classical screening methods.

Future research should morely motivate on advancing the reliability across diverse clinical settings in the real world. The generalizability and clinical applicability of the proposed models with multi-center datasets can be studied further to perform external validation. The integration of additional clinical information, such as patient demographics, corneal biomechanical properties, and longitudinal follow-up measurements, may further improve severity prediction accuracy.Beyond that, future studies may incorporate raw corneal images and advanced deep learning architectures to automatically extract novel biomarkers complementing the currently used manual features. Explainable artificial intelligence methods should also be explored to enhance model transparency and provide clinicians evidential interpretations to support predictions. Ultimately, combining longitudinal data analysis, bilateral eye assessment, and advanced machine learning techniques may enable more accurate early detection, personalized monitoring, and improved management of KC progression.

Declarations

Funding

The authors received no specific funding for this work.

Competing interests

The authors have declared that no competing interests exist.

Ethics approval and consent to participate

Not applicable. The study relies entirely on a publicly available, fully anonymized dataset and no direct human or animal subjects were involved.

Consent for publication

Not applicable. This manuscript does not contain any individual person's data in the form of identifiable images, videos, or text.

Data availability

The dataset is publicly available at: https://github.com/DM2LL/Cornea and Harvard Dataverse(https://dataverse.harvard.edu/dataset.xhtml?persistentId=doi:10.7910/DVN/G2CRMO).

Author contribution

STO developed the methodology and analyzed the results, wrote the code, prepared the data, which was publicly available at conducted the experiments and the associated analysis, completed the writing, editing and approval of the manuscript.

Appendix A The most important 50 features with scores by using F-test method.

Table A1: The most important 50 features with scores by using F-test method.

Steepest.1	496,932
Steepest.Posterior.	496,932
Steepest.3	496,932
Score.Posterior.	444,763
Result.4	276,7185
Asy..Posterior.	223,8471
Asymmetry.5	223,8471
Score.Anterior.	222,2534
DSI.5mm..1	211,8617
K.Max..8mm..1	206,3441
DSI.6mm..1	205,9888
K.Max..10mm..1	202,6955
DSI.4mm..1	201,1366
SD_P.4mm..1	199,8513
SAI.1	199,1972
SAI	193,462
SAI.2	188,5452
Asymmetry.3	186,546
Asymmetry.1	186,5365
Asy..Keratometric.	186,5365
Result.2	184,3704
Asymmetry.7	183,9768
Asymmetry.4	177,4037
Asymmetry.2	169,77
Asymmetry	169,7567
OSI.6mm..1	166,2268
OSI.5mm..1	166,2063
DSI.6mm..2	164,8354
Result.6	164,4538
Asymmetry.6	164,2059
CV_P.4mm..1	163,9766
DSI.5mm..2	163,6298
DSI.6mm.	160,8435
OSI.6mm.	160,5511
DSI.5mm.	160,2679
OSI.4mm..1	158,2431
OSI.5mm.	156,2806
OSI.6mm..2	156,2633

DSI.4mm..2	155,6
DSI.4mm.	152,8313
OSI.5mm..2	149,4589
SD_P.4mm..2	147,77
OSI.4mm.	142,3597
DSI.9mm..1	141,2452
SD_P.4mm.	140,9942
OSI.4mm..2	137,6194
CV_P.4mm..2	127,2268
OSI.9mm..1	120,7626
CV_P.4mm.	120,1427
Thinnest	118,8561

References

[1] Yang, Y., Pavlatos, E., Chamberlain, W., Huang, D., Li, Y.: Keratoconus detection using oct corneal and epithelial thickness map parameters and patterns. Journal of Cataract & Refractive Surgery **47**(6), 759–766 (2021)

[2] Falgayrettes, N., Patoor, E., Cleymand, F., Zevering, Y., Perone, J.-M.: Biomechanics of keratoconus: Two numerical studies. PLoS One **18**(2), 0278455 (2023)

[3] Singh, R.B., Koh, S., Sharma, N., Woreta, F.A., Hafezi, F., Dua, H.S., Jhanji, V.: Keratoconus. Nature Reviews Disease Primers **10**(1), 81 (2024)

[4] Espandar, L.M.J.: Keratoconus: Overview and update on treatment. Middle East African Journal of Ophthalmology **17**(1), 15–20 (2010)

[5] H, K., JY, C., S, S., EW, C., S, W., SL., W.: Crosslinking improves the quality of life of people with keratoconus: A crosssectional and longitudinal study from the save sight keratoconus registry. Cornea **42(11)**(11), 1377–1383 (2023)

[6] Gorskova, E., Sevost'Ianov, E.: Epidemiology of keratoconus in the urals. vestnik oftalmologii **114**(4), 38–40 (1998)

[7] Jonas, J.B., Nangia, V., Matin, A., Kulkarni, M., Bhojwani, K.: Prevalence and associations of keratoconus in rural maharashtra in central india: the central india eye and medical study. American journal of ophthalmology **148**(5), 760–765 (2009)

[8] Kennedy, R.H., Bourne, W.M., Dyer, J.A.: A 48-year clinical and epidemiologic study of keratoconus. American journal of ophthalmology **101**(3), 267–273 (1986)

[9] Gomes, J.A., Rodrigues, P.F., Lamazales, L.L.: Keratoconus epidemiology: A review. Saudi Journal of Ophthalmology **36**(1), 3–6 (2022)

[10] Hashemi, H., Heydarian, S., Hooshmand, E., Saatchi, M., Yekta, A., Aghamirsalim, M., Valadkhan, M., Mortazavi, M., Hashemi, A., Khabazkhoob, M.: The prevalence and risk factors for keratoconus: a systematic review and meta-analysis. Cornea **39**(2), 263–270 (2020)

[11] Godefrooij, D.A., De Wit, G.A., Uiterwaal, C.S., Imhof, S.M., Wisse, R.P.: Age-specific incidence and prevalence of keratoconus: a nationwide registration study. American journal of ophthalmology **175**, 169–172 (2017)

[12] Barbara, R., Turnbull, A.M., Malem, A., Anderson, D.F., Hossain, P., Konstantopoulos, A., Barbara, A.: Epidemiology of keratoconus. Controversies in the Management of Keratoconus, 1–16 (2019)

[13] Santodomingo-Rubido, J., Carracedo, G., Suzaki, A., Villa-Collar, C., Vincent, S.J., Wolffsohn, J.S.: Keratoconus: An updated review. Contact Lens and Anterior Eye **45**(3), 101559 (2022)

[14] Li, Y., Meisler, D.M., Tang, M., Lu, A.T., Thakrar, V., Reiser, B.J., Huang, D.: Keratoconus diagnosis with optical coherence tomography pachymetry mapping. Ophthalmology **115**(12), 2159–2166 (2008)

[15] Niazi, S., Jiménez-García, M., Findl, O., Gatzioufas, Z., Doroodgar, F., Shahriari, M.H., Javadi, M.A.: Keratoconus diagnosis: from fundamentals to artificial intelligence: a systematic narrative review. Diagnostics **13**(16), 2715 (2023)

[16] Fan, L., Kandel, H., Watson, S.L.: Impacts of keratoconus on quality of life: a qualitative study. Eye **38**(16), 3136–3144 (2024)

[17] Institute, N.E.: Corneal Dystrophies. https://www.nei.nih.gov/learn-about-eye-health/eye-conditions-and-diseases/corneal-conditions/corneal-dystrophies/. [Online; accessed 01-Febryary-2025] (2024)

[18] Sharma, N.: Advancements in Keratoconus Management. LWW (2024)

[19] Saad, A., Debellemanière, G., Zeboulon, P., Rizk, M., Rouger, H., Mazharian, A., Grise-Dulac, A., Panthier, C., Gatinel, D.: Discrimination between keratoconus, forme fruste keratoconus, and normal eyes using a novel oct-based tomographer. Journal of Cataract & Refractive Surgery **49**(11), 1092–1097 (2023)

[20] Hoffmann, P.C., Abraham, M., Hirnschall, N., Findl, O.: Prediction of residual astigmatism after cataract surgery using swept source fourier domain optical coherence tomography. Current Eye Research **39**(12), 1178–1186 (2014)

[21] Zarei-Ghanavati, S., Moghaddam, M.S., Bakhtiari, E., Shirzad, S., Sadeghi, J., Shariati, M.M.: Agreement between placido disc, scheimpflug, and optical coherence tomography-based measurements of corneal topography in healthy myopic individuals. Journal of Current Ophthalmology **36**(3), 272–278 (2024)

[22] McMahon, T.T., Szczotka-Flynn, L., Barr, J.T., Anderson, R.J., Slaughter, M.E., Lass, J.H., Iyengar, S.K., Group, C.S., *et al.*: A new method for grading the severity of keratoconus: the keratoconus severity score (kss). Cornea **25**(7), 794–800 (2006)

[23] Belin, M.W., Kundu, G., Shetty, N., Gupta, K., Mullick, R., Thakur, P.: Abcd: A new classification for keratoconus. Indian journal of ophthalmology **68**(12), 2831–2834 (2020)

[24] Ortiz-Toquero, S., Martin, R.: Keratoconus screening in primary eye care–a general overview. Eur Ophthalmic Rev **10**(2), 80 (2016)

[25] Belin, M., Duncan, J.: Keratoconus: the abcd grading system. Klinische Monatsblätter für Augenheilkunde **233**(06), 701–707 (2016)

[26] Burns, D., Johnston, F., Frazer, D., Patterson, C., Jackson, A.: Keratoconus: an analysis of corneal asymmetry. British Journal of Ophthalmology **88**(10), 1252–1255 (2004)

[27] Rabinowitz, Y.S.: Keratoconus. Survey of ophthalmology **42**(4), 297–319 (1998)

[28] Romero-Jiménez, M., Santodomingo-Rubido, J., Wolffsohn, J.S.: Keratoconus: a review. Contact Lens and Anterior Eye **33**(4), 157–166 (2010)

[29] Tur, V.M., MacGregor, C., Jayaswal, R., O'Brart, D., Maycock, N.: A review of keratoconus: diagnosis, pathophysiology, and genetics. Survey of ophthalmology **62**(6), 770–783 (2017)

[30] Ferdi, A.C., Nguyen, V., Gore, D.M., Allan, B.D., Rozema, J.J., Watson, S.L.: Keratoconus natural progression: a systematic review and meta-analysis of 11 529 eyes. Ophthalmology **126**(7), 935–945 (2019)

[31] Bobkova, D.: Keratoconus: modern diagnostic aspects and classification issues. Pacific Medical Journal **1**(3 (89)), 13–18 (2022)

[32] Doctor, K., Vunnava, K.P., Shroff, R., Kaweri, L., Lalgudi, V.G., Gupta, K., Kundu, G.: Simplifying and understanding various topographic indices for keratoconus using scheimpflug based topographers. Indian Journal of Ophthalmology **68**(12), 2732–2743 (2020)

[33] Muhsin, Z.J., Qahwaji, R., Ghafir, I., AlShawabkeh, M., Al Bdour, M., AlRyalat, S.A., Al-Taee, M.: Highly efficient stacking ensemble learning model for automated keratoconus screening. Eye and Vision **12**(1), 25 (2025)

[34] Maile, H., Li, J.-P.O., Gore, D., Leucci, M., Mulholland, P., Hau, S., Szabo, A., Moghul, I., Balaskas, K., Fujinami, K., Hysi, P., Davidson, A., Liskova, P., Hardcastle, A., Tuft, S., Pontikos, N.: Machine learning algorithms to detect subclinical keratoconus: Systematic review. JMIR Med Inform **9**(12), 27363 (2021) https://doi.org/10.2196/27363

[35] Yousefi, S.: Replication Data for the "Keratoconus severity identification using unsupervised machine learning", Siamak Yousefi, Ebrahim Yousefi, Hidenori Takahashi, Takahiko Hayashi, Hironobu Tampo, Satoru Inoda, Yusuke Arai, and Penny Asbell, PLOS One 2018. Harvard Dataverse. Accessed on 2024-07-2024 (2018). https://doi.org/10.7910/DVN/G2CRMO . https://doi.org/10.7910/DVN/G2CRMO

[36] Yousefi, S., Yousefi, E., Takahashi, H., Hayashi, T., Tampo, H., Inoda, S., Arai, Y., Asbell, P.: Keratoconus severity identification using unsupervised machine

learning. PLoS One **13**(11), 0205998 (2018)

[37] Mirsalehi, M., Fassbind, B., Streich, A., Langenbucher, A.: Prediction of the ectasia screening index from raw casia2 volume data for keratoconus identification by using convolutional neural networks. PloS one **20**(9), 0311036 (2025)

[38] Maeda, N., Klyce, S.D., Smolek, M.K.: Neural network classification of corneal topography. preliminary demonstration. Investigative ophthalmology & visual science **36**(7), 1327–1335 (1995)

[39] Smolek, M.K., Klyce, S.D.: Current keratoconus detection methods compared with a neural network approach. Investigative ophthalmology & visual science **38**(11), 2290–2299 (1997)

[40] Accardo, P.A., Pensiero, S.: Neural network-based system for early keratoconus detection from corneal topography. Journal of biomedical informatics **35**(3), 151–159 (2002)

[41] Carvalho, L.A.V.d., Barbosa, M.S.: Neural networks and statistical analysis for classification of corneal videokeratography maps based on zernike coefficients: a quantitative comparison. Arquivos brasileiros de oftalmologia **71**, 337–341 (2008)

[42] Silverman, R.H., Urs, R., RoyChoudhury, A., Archer, T.J., Gobbe, M., Reinstein, D.Z.: Epithelial remodeling as basis for machine-based identification of keratoconus. Investigative ophthalmology & visual science **55**(3), 1580–1587 (2014)

[43] Muhsin, Z., Qahwaji, R., Ghafir, I., AlShawabkeh, M., Al Bdour, M., AlRyalat, S.A., AlTaee, M.: Two-stage ensemble learning framework for automated classification of keratoconus severity. Available at SSRN 5096562 (2025)

[44] Muhsin, Z.J., Qahwaji, R., Ghafir, I., Al Bdour, M., AlRyalat, S., AlShawabkeh, M., Al-Taee, M.: Performance comparison of machine learning algorithms for keratoconus detection. In: 2024 IEEE 30th International Conference on Telecommunications (ICT), pp. 01–06 (2024). IEEE

[45] Subramanian, P., Ramesh, G., Parameshachari, B.: Comparative analysis of machine learning approaches for the early diagnosis of keratoconus. Distributed Computing and Optimization Techniques: Select Proceedings of ICDCOT 2021, 241–250 (2022)

[46] Mustapha, A., Mohamed, L., Hamid, H., Ali, K.: Machine learning techniques in keratoconus classification: a systematic review. International Journal of Advanced Computer Science and Applications **14**(5) (2023)

[47] Sandhiya, R., Chakkravthi, N.M., Vignesh, D.N., Chander, R.S.: Keratoconus detection using machine learning. In: 2024 3rd International Conference on

Artificial Intelligence For Internet of Things (AIIoT), pp. 1–6 (2024). IEEE

[48] Souza, M.B., Medeiros, F.W., Souza, D.B., Garcia, R., Alves, M.R.: Evaluation of machine learning classifiers in keratoconus detection from orbscan ii examinations. Clinics **65**(12), 1223–1228 (2010)

[49] Smadja, D., Touboul, D., Cohen, A., Doveh, E., Santhiago, M.R., Mello, G.R., Krueger, R.R., Colin, J.: Detection of subclinical keratoconus using an automated decision tree classification. American journal of ophthalmology **156**(2), 237–246 (2013)

[50] Cao, K., Verspoor, K., Sahebjada, S., Baird, P.N.: Evaluating the performance of various machine learning algorithms to detect subclinical keratoconus. Translational Vision Science & Technology **9**(2), 24–24 (2020)

[51] Shi, C., Wang, M., Zhu, T., Zhang, Y., Ye, Y., Jiang, J., Chen, S., Lu, F., Shen, M.: Machine learning helps improve diagnostic ability of subclinical keratoconus using scheimpflug and oct imaging modalities. Eye and Vision **7**, 1–12 (2020)

[52] Issarti, I., Consejo, A., Jiménez-García, M., Hershko, S., Koppen, C., Rozema, J.J.: Computer aided diagnosis for suspect keratoconus detection. Computers in biology and medicine **109**, 33–42 (2019)

[53] Lavric, A., Valentin, P.: Keratodetect: keratoconus detection algorithm using convolutional neural networks. Computational intelligence and neuroscience **2019**(1), 8162567 (2019)

[54] Lavric, A., Anchidin, L., Popa, V., Al-Timemy, A.H., Alyasseri, Z., Takahashi, H., Yousefi, S., Hazarbassanov, R.M.: Keratoconus severity detection from elevation, topography and pachymetry raw data using a machine learning approach. Ieee Access **9**, 84344–84355 (2021)

[55] Kamiya, K., Ayatsuka, Y., Kato, Y., Fujimura, F., Takahashi, M., Shoji, N., Mori, Y., Miyata, K.: Keratoconus detection using deep learning of colour-coded maps with anterior segment optical coherence tomography: a diagnostic accuracy study. BMJ open **9**(9), 031313 (2019)

[56] Chen, X., Zhao, J., Iselin, K.C., Borroni, D., Romano, D., Gokul, A., McGhee, C.N., Zhao, Y., Sedaghat, M.-R., Momeni-Moghaddam, H., et al.: Keratoconus detection of changes using deep learning of colour-coded maps. BMJ open ophthalmology **6**(1) (2021)

[57] Xie, Y., Zhao, L., Yang, X., Wu, X., Yang, Y., Huang, X., Liu, F., Xu, J., Lin, L., Lin, H., *et al.*: Screening candidates for refractive surgery with corneal tomographic–based deep learning. JAMA ophthalmology **138**(5), 519–526 (2020)

[58] Kuo, B.-I., Chang, W.-Y., Liao, T.-S., Liu, F.-Y., Liu, H.-Y., Chu, H.-S., Chen,

W.-L., Hu, F.-R., Yen, J.-Y., Wang, I.-J.: Keratoconus screening based on deep learning approach of corneal topography. Translational Vision Science & Technology **9**(2), 53–53 (2020)

[59] Xu, Z., Feng, R., Jin, X., Hu, H., Ni, S., Xu, W., Zheng, X., Wu, J., Yao, K.: Evaluation of artificial intelligence models for the detection of asymmetric keratoconus eyes using scheimpflug tomography. Clinical & Experimental Ophthalmology **50**(7), 714–723 (2022)

[60] Feng, R., Xu, Z., Zheng, X., Hu, H., Jin, X., Chen, D.Z., Yao, K., Wu, J.: Kernet: a novel deep learning approach for keratoconus and sub-clinical keratoconus detection based on raw data of the pentacam hr system. IEEE Journal of Biomedical and Health Informatics **25**(10), 3898–3910 (2021)

[61] Al-Timemy, A.H., Alzubaidi, L., Mosa, Z.M., Abdelmotaal, H., Ghaeb, N.H., Lavric, A., Hazarbassanov, R.M., Takahashi, H., Gu, Y., Yousefi, S.: A deep feature fusion of improved suspected keratoconus detection with deep learning. Diagnostics **13**(10), 1689 (2023)

[62] Abdelmotaal, H., Hazarbasanov, R.M., Salouti, R., Nowroozzadeh, M.H., Taneri, S., Al-Timemy, A.H., Lavric, A., Takahashi, H., Yousefi, S.: A hybrid transformers-based convolutional neural network model for keratoconus detection in scheimpflug-based dynamic corneal deformation videos. Journal of Ophthalmic & Vision Research **20**, 10–18502 (2025)

[63] Reddy, J.C., Bhamidipati, P., Dwivedi, S., Dhara, K.K., Joshi, V., Hasnat Ali, M., Vaddavalli, P.K.: Kedop: Keratoconus early detection of progression using tomography images. European journal of ophthalmology **32**(5), 2554–2564 (2022)

[64] Quanchareonsap, W., Kasetsuwan, N., Reinprayoon, U., Piyacomn, Y., Wungcharoen, T., Jermjutitham, M.: Deep learning algorithm for keratoconus detection from tomographic maps and corneal biomechanics: A diagnostic study. Journal of Current Ophthalmology **36**(1), 46–53 (2024)

[65] Syta, A., Podkowiński, A., Chorągiewicz, T., Karpiński, R., Gęca, J., Wróbel-Dudzińska, D., Jonak, K.E., Głuchowski, D., Maciejewski, M., Rejdak, R., *et al.*: Machine learning-assisted early detection of keratoconus: a comparative analysis of corneal topography and biomechanical data. Scientific Reports **15**(1), 24399 (2025)

[66] Jameel, S.K., Aydin, S., Ghaeb, N.H.: Machine learning techniques for corneal diseases diagnosis: a survey. International Journal of Image and Graphics **21**(02), 2150016 (2021)

[67] Maile, H., Li, J.-P.O., Gore, D., Leucci, M., Mulholland, P., Hau, S., Szabo, A., Moghul, I., Balaskas, K., Fujinami, K., *et al.*: Machine learning algorithms to detect subclinical keratoconus: systematic review. JMIR medical informatics

9(12), 27363 (2021)

[68] Goodman, D., Zhu, A.Y.: Utility of artificial intelligence in the diagnosis and management of keratoconus: a systematic review. Frontiers in Ophthalmology **4**, 1380701 (2024)

[69] Spira, C., Grigoryan, A., Szentmary, N., Seitz, B., Langenbucher, A., Eppig, T.: Comparison of the specificity and sensitivity of various instrument-guided keratoconus indices and classifiers. Der Ophthalmologe **112**, 353–358 (2015)

[70] Computation, N.: Long short-term memory. Neural Comput **9**, 1735–1780 (2016)

[71] Gomariz, A., Campos, M., Marin, R., Goethals, B.: Clasp: An efficient algorithm for mining frequent closed sequences. In: Pacific-Asia Conference on Knowledge Discovery and Data Mining, pp. 50–61 (2013). Springer

[72] Fournier-Viger, P., Lin, J.C.-W., Gomariz, A., Gueniche, T., Soltani, A., Deng, Z., Lam, H.T.: The spmf open-source data mining library version 2. In: Joint European Conference on Machine Learning and Knowledge Discovery in Databases, pp. 36–40 (2016). Springer

[73] Schubert, E., Lenssen, L.: Fast k-medoids clustering in rust and python. Journal of Open Source Software **7**(75), 4183 (2022)

[74] Maeno, S., Koh, S., Inoue, R., Oie, Y., Maeda, N., Jhanji, V., Nishida, K.: Fourier analysis on irregular corneal astigmatism using optical coherence tomography in various severity stages of keratoconus. American Journal of Ophthalmology **243**, 55–65 (2022)

[75] Elmassry, A., Osman, A., Sabry, M., Elmassry, M., Katkat, M., Hatata, M.Y., El-Kateb, M.: Corneal endothelial cells changes in different stages of keratoconus: a multi-centre clinical study. BMC ophthalmology **21**(1), 143 (2021)